This .pdf file contains:

Supplementary Notes 1–8

Supplementary Figures 1–9

Supplementary References

Table of Contents

Supplementary Note 1: Detailed information on erythritol and antioxidants

To compare the antioxidative efficacy, six antioxidants were pre-screened and their effects on improving the thermal stability of erythritol were verified. The antioxidants were categorized as follows: two hindered phenol antioxidants (AO1010, AO1098); two phosphite antioxidants (THP-EPQ, THP-24); and the composite blends AO-B215 and AO-B225, which are comprised of hindered phenol AO1010 and phosphite AO168. The prices of the materials were obtained from the official websites of the manufacturers. The specific information about erythritol and the six antioxidants is given in Supplementary Table 1.

Supplementary Table 1. Detailed information on erythritol and the antioxidants.

Category	Material	Chemical formula	CAS No.	CAS No.	Purity (%)	Price (¥/g)
	erythritol	$C_4H_{10}O_4$	149-32-6	Macklin	99%	1.7
hindered phenolics	AO1010	$C_{73}H_{108}O_{12}$	6683-19-8	Kai We	98%	0.8
	AO1098	$C_{40}H_{64}N_2O_4$	23128-74-7	Ron	98%	1.6
	THP-EPQ	$C_{68}H_{92}O_4P_2$	38613-77-3	Macklin	98%	7.2
phosphites	THP-24	$C_{33}H_{50}O_6P_2$	26741-53-7	Yuanye	94%	1.6
	AO168	$C_{42}H_{63}O_3P$	31570-04-4	Macklin	98%	0.9
Composites	AO-B215	67%AO168+ 33%AO1010		BASF		0.04
	AO-B225	50%AO168+ 50%AO1010		Macklin		0.5

The molecular structures of erythritol and the six antioxidants are depicted below in Supplementary Fig. 1.

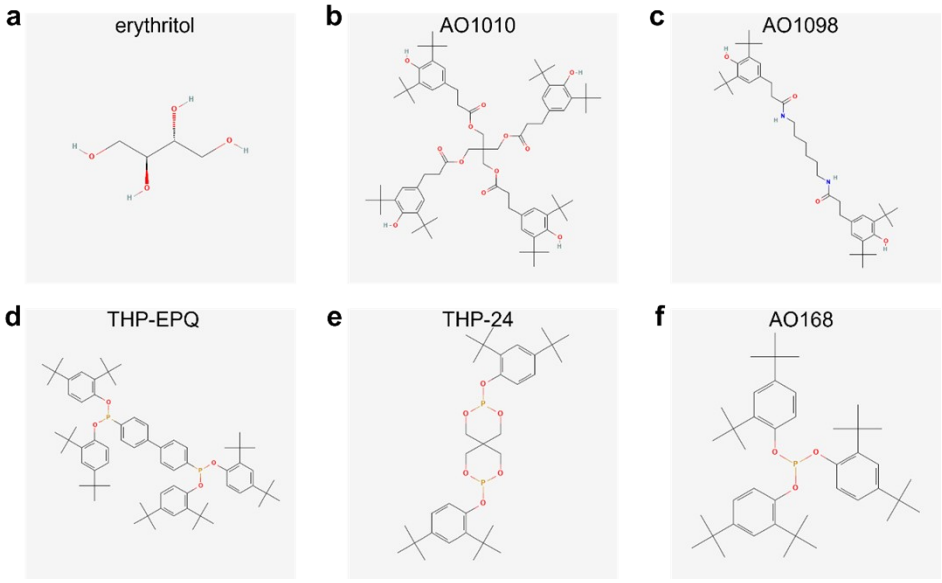

Supplementary Fig. 1. Chemical structures of erythritol and the five antioxidants investigated in this study: (a) erythritol, (b) AO1010, (c) AO1098, (d) THP-EPQ, (e) THP-24, and (f) AO168.

Since mixing methods can influence antioxidant efficacy, two approaches were compared (Supplementary Fig. 2). Mechanical grinding of Antioxidant 1010 and erythritol resulted in a heterogeneous suspension with surface aggregation. Conversely, melt-blending achieved a highly uniform dispersion without flotation. This homogeneity directly translates to enhanced antioxidant efficacy, making melt-blending the preferred preparation method in this study.

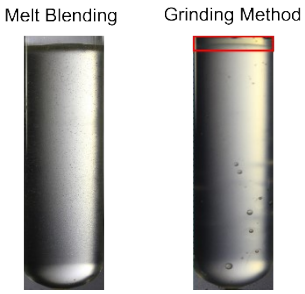

Supplementary Fig. 2. Dispersion states of the antioxidant within erythritol prepared by two different methods.

Supplementary Note 2: Stability of erythritol under different operating conditions

2.1 Thermal stability of pristine erythritol under different degrees of superheat

The changes in the melting enthalpy of erythritol with heating duration under different degrees of superheat (ΔT_{sh} = 30°C, 60°C, and 90°C) are shown in Supplementary Fig. 3. As the superheat increases from 30°C to 90°C, the melting enthalpy degradation rate becomes more pronounced. At a superheat of 30°C, after 100 h of thermal-aging, the melting enthalpy decreases from 333.7±1.2 J/g to 314±5.7 J/g, representing a decline of 4.8%. When the superheat is 60°C, the melting enthalpy decreases by 13.1% to 286.9±0.8 J/g over the same duration of 100 h, which is nearly 2.8 times the decline observed at 30°C. Most notably, at the superheat of 90°C, the enthalpy plummets by ~37.3% to 206.8±5.7 J/g after heated for 100 h. This loss magnitude is 7.8 times and 2.9 times higher than that observed at 30°C and 60°C, respectively, indicating that excessive charging temperatures must be avoided in practical applications.

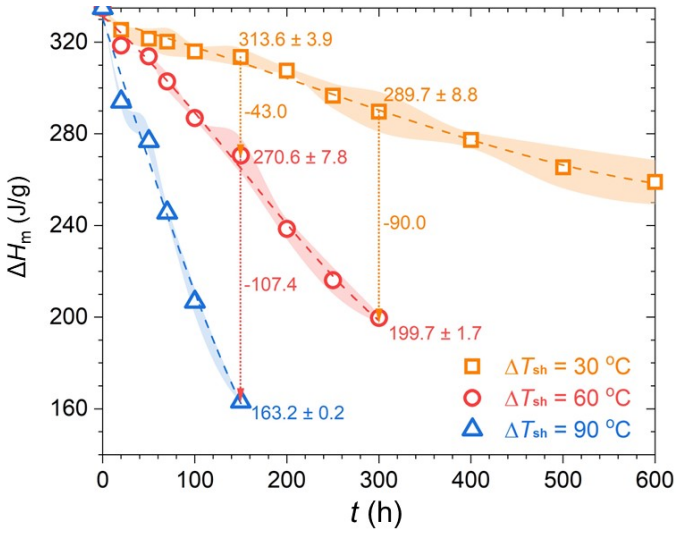

Supplementary Fig. 3. Changes in the melting enthalpy of erythritol with time when heated at the degrees of superheat of 30°C, 60°C, and 90°C.

2.2 Cycling stability of pristine erythritol under different degrees of superheat

To characterize the cycling stability of erythritol, a unified enthalpy $\Delta H_n/\Delta H_0$ was used to represent the TES performance change during the cycling process, where ΔH_n is the melting enthalpy of the sample after multiple cycles, ΔH_0 is the melting enthalpy of the initial sample, and subscript n denotes the number of cycles.

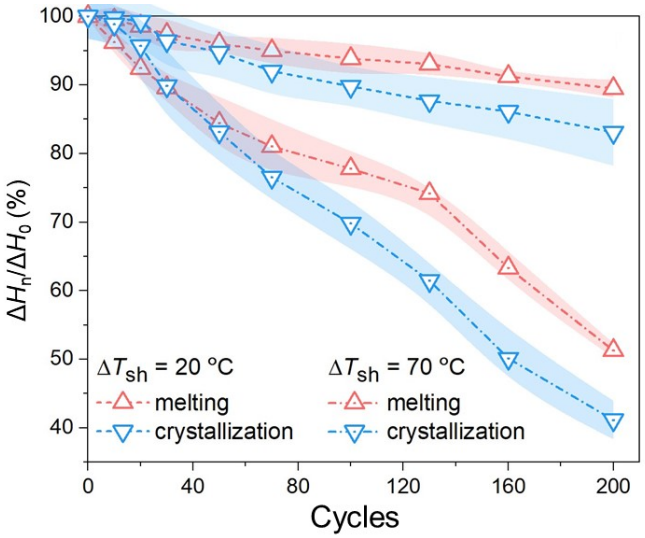

Supplementary Fig. 4. Evolutions of the melting and crystallization enthalpies of erythritol over multiple cycles at the degrees of superheat of 20°C and 70°C.

As depicted in Supplementary Fig. 4, the ratio $\Delta H_n/\Delta H_0$ for both melting and crystallization enthalpies exhibits a progressive decline with increasing the cycle number. Notably, at a high superheat of 70°C, the enthalpy ratio of erythritol decreases to approximately half, reaching ~51.3%. Regarding crystallization enthalpy, the degradation rate is even faster as cycling progresses. The ratio drops to a mere ~41.2% after 200 cycles. At a moderate superheat of 20°C, the degradation kinetics is markedly decelerated compared to the 70°C condition: after 200 cycles,

the $\Delta H_n/\Delta H_0$ values for melting and crystallization decline by only ~10.5% and ~16.9%, respectively. These findings clearly indicate that the intrinsic thermal stability of erythritol is poor that cannot satisfy the requirements for practical TES applications.

2.3 Changes in the melting enthalpy of erythritol with different loadings of AO1010

Supplementary Fig. 5 illustrates the temporal evolution of melting enthalpy for erythritol systems incorporating varying loadings of AO1010 (i.e., 0.01, 0.1, 1, and 2 wt.%) when heated at the degrees of superheat of 30°C, 60°C, and 90°C. The results demonstrate that the melting enthalpies of erythritol with different addition amounts of AO1010 are 335 J/g, 333.3 J/g, 330.6 J/g, and 328.7 J/g, respectively. The AO1010 provides outstanding protection for erythritol at low superheating levels, but as the heating temperature increases, the antioxidative capacity of AO1010 gradually fails. Following a 600 h thermal aging at a superheat of 30°C, the melting enthalpy of erythritol incorporated with 0.01 wt.% AO1010 exhibits a minor decline of only ~39.9 J/g. However, at elevated superheats of 60°C and 90°C, the enthalpy loss intensifies significantly to ~105.9 J/g and ~131.5 J/g, respectively. With increasing the AO1010 concentration to 0.1, 1, and 2 wt.%, the corresponding enthalpy reductions after 600 h at 30°C are further restricted to 35.9 J/g, 29.3 J/g, and 29.6 J/g, respectively.

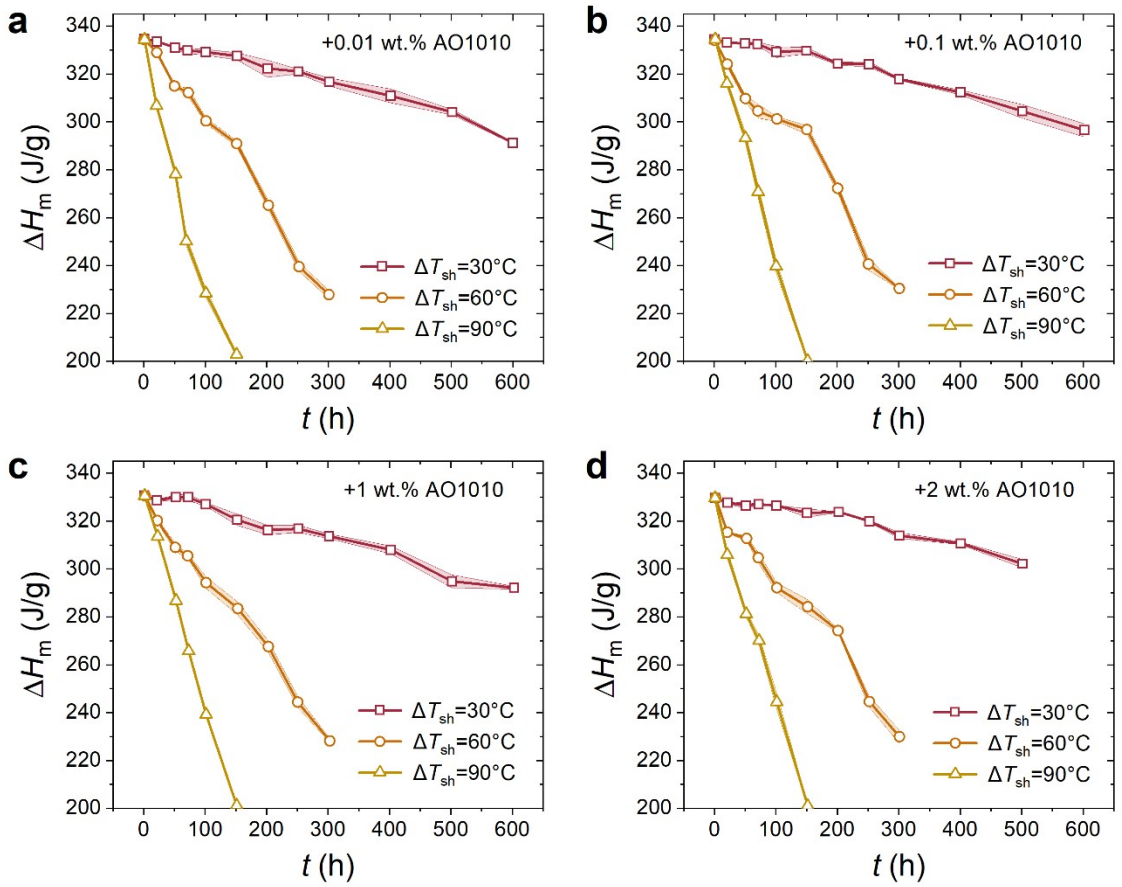

Supplementary Fig. 5. Changes in the melting enthalpy for erythritol with varying AO1010 loadings when heated at the degrees of superheat of 30°C, 60°C, and 90°C: (a) 0.01 wt.%, (b) 0.1 wt.%, (c) 1 wt.%, and (d) 2 wt.%.

Supplementary Note 3: Cycling stability of sugar alcohols from existing literature

Methods for evaluating the cyclic stability of sugar alcohols include the temperature history curve method and non-isothermal DSC testing. Test results for the cyclic stability of sugar alcohol PCMs from various literature sources are shown in Supplementary Table 2, where the temperatures in the test conditions represent the superheat.

Supplementary Table 2. Test results of the cyclic stability of sugar alcohol PCMs across different literature sources.

Test Methods	Test Conditions	Materials	Cycles	$\Delta H_{m,n}/\Delta H_{m,0}$	References
T-history	20°C	Erythritol	70	0.949	1
			200	0.891	
	70°C	Erythritol	70	0.811	1
			130	0.740	
			200	0.513	
	20°C	D-mannitol	50	0.845	1
			100	0.696	
			160	0.514	
	20°C	D-dulcitol	20	0.789	1
			70	0.499	
	20°C	Inositol	145	0.924	1
			200	0.897	

	12°C, N_2	Erythritol	40 100	0.998 0.999	2
	30°C	D-mannitol	50	0.424	3
	30°C	Inositol	100	0.891	3
DSC	42°C	Erythritol	100	0.976	4
	12°C	Erythritol	200	0.995	5

Supplementary Note 4: Lifetime projection for dual-protected erythritol

To predict the cycling life of both pristine erythritol and erythritol under the dual-protection strategy, we performed numerical fitting on the 1,000-cycle datasets presented in Fig. 2h. The fitting equations are given, respectively, as follows:

$$\frac{\Delta H_{m,n}}{\Delta H_{m,0}} = -2\times10^{-5}n^2 - 6.85\times10^{-2}n + 334.24 \quad \text{(S-1)}$$

$$\frac{\Delta H_{m,n}}{\Delta H_{m,0}} = -3\times10^{-5}n^2 - 3.8\times10^{-3}n + 330.04 \quad \text{(S-2)}$$

where n denotes the number of thermal cycles.

As illustrated in Supplementary Fig. 6, a comparison between the experimental data and the numerical fitting curves reveals good correlations for both the pristine and dual-protected cases, with R^2 values of 0.9957 and 0.9924, respectively. Under the dual-protected strategy, the projected lifespan of erythritol exceeds 1,400 cycles for an 80% capacity retention threshold.

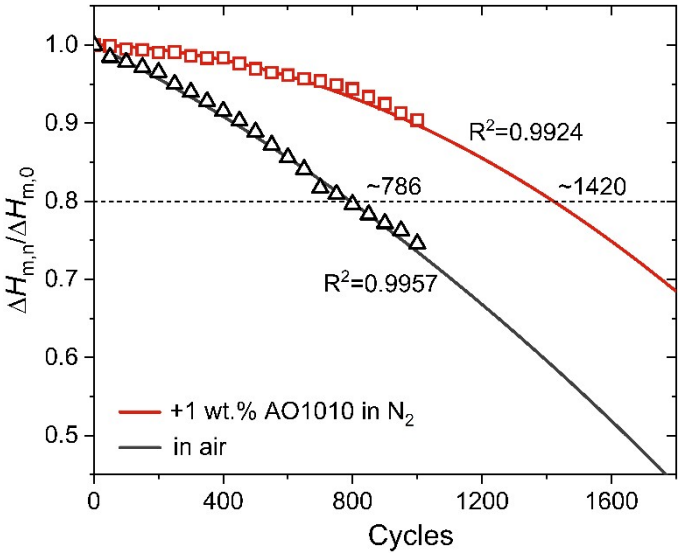

Supplementary Fig. 6. Predicted thermal cycling lifespan and fitting curves for erythritol under unprotected and dual-protection strategies under the superheat of 30°C.

Supplementary Note 5: Techno-economic analysis on different protection strategies

To quantify the impact of different protection strategies on the levelized cost of storage (LCOS), we conducted a techno-economic analysis based on a 1 MWh industrial-scale erythritol-based thermal battery. The study compares the costs of three configurations: industrial nitrogen with 1 wt.% AO1010 (Scenario A), argon with 1 wt.% AO1010 (Scenario B), and high-purity nitrogen protection (Scenario C). The total system cost G (\$/kWh) was calculated based on the modified Kocher model[6]:

$$G = \frac{G_{\text{PCM-total}} + G_{\text{Container}} + G_{\text{Gas-maintain}}}{E_{\text{stored}} \cdot \eta_{\text{deg}}} + G_{\text{hx}} \tag{S-3}$$

where $G_{\text{PCM-total}}$ represents the total composite material cost (including antioxidants), G_{hx} denotes the total heat exchanger system cost (\$), $G_{\text{Container}}$ signifies the tank and sealing system cost (dependent on airtightness requirements), $G_{\text{Gas-maintain}}$ covers gas replacement and full lifecycle replenishment costs, E_{stored} indicates the theoretical TES capacity (1 MWh), and η_{deg} reflects the full lifecycle capacity retention rate (a key factor proposed by Lim et al.[7]).

For the purpose of this comparative analysis, a uniform effective capacity retention of 83% after 10,000 h (a period during which the material's lifespan satisfies operational requirements even under three daily cycles) was assumed across all three scenarios, while the combined cost of the heat exchangers and insulation (G_{hx}) was held constant at 35 \$/kWh. The total material cost of the composite PCM comprises the expenses for both erythritol and the AO1010 additive. We assumed unit prices of 2.8 \$/kg for industrial-grade pure erythritol and 14 \$/kg for AO1010, with the latter incorporated at a loading of 1 wt.%. Based on the initial melting enthalpy of 335 J/g for

erythritol, the material cost without the antioxidant is 30,088.8 $, while the cost with the antioxidant is 31,292.4 $. Since antioxidants can eliminate trace oxygen, the system's airtightness requirements are reduced, allowing for the use of industrial-grade sealant $G_{\text{seal-low}}$ (2,800 $) and inexpensive industrial nitrogen (0.14 $/m^3).

Assuming a total lifecycle gas requirement of 200 m^3 (including initial filling and infrequent replenishment), the LCOS for Scenario A is 83.3 $/kWh. Scenario B employs argon, the most inert noble gas, in conjunction with the AO1010. Although this configuration offers superior protection, the prohibitive cost of argon—15 times that of nitrogen—necessitates the deployment of high-hermeticity containment vessels (8,400 $) to mitigate gas loss and reduce operational expenditures. Consequently, the LCOS for Scenario B is 90.5 $/kWh, representing a 25.5% increase compared to the use of nitrogen and AO1010. In Scenario C, while the exclusive reliance on high-purity nitrogen eliminates the cost of antioxidants, achieving an equivalent capacity retention of 83% necessitates the deployment of high-purity nitrogen coupled with high-hermeticity containment vessels to strictly preclude the leakage of external oxygen. Consequently, this configuration yields a LCOS of 88.7 $/kWh, representing a 6.5% cost increase relative to the nitrogen-AO1010 dual-protection strategy.

In conclusion, a comprehensive techno-economic assessment of a 1 MWh industrial-scale TES system identifies Scenario A (nitrogen + AO1010) as the economically optimal solution, achieving the lowest LCOS at 83.3 $/kWh. Although the incorporation of antioxidants incurs a marginal increase in raw material costs (approximately 1,203.6 $), its function as an effective “chemical soldier” unlocks the feasibility of utilizing low-cost industrial nitrogen and standard

sealing configurations. This approach yields substantial savings in atmosphere and containment costs compared to Scenario B (90.5 $/kWh), which relies on prohibitively expensive argon and high-hermeticity vessels. Moreover, the comparison with Scenario C (88.7 $/kWh) exposes a 'hidden cost trap': while omitting additives eliminates specific material expenses, the rigorous requirement for expensive high-purity gas and high-hermeticity containment induces a 6.5% surge in the unit energy cost. Ultimately, the employment of both nitrogen and AO1010 leverages a negligible marginal material input to secure the dual benefits of low-cost atmosphere substitution and life-cycle capacity retention, showcasing an economic advantage for large-scale practical applications.

Supplementary Note 6: The antioxidative efficacy of AO1010 on other sugar alcohols

The thermal stability profiles of different sugar alcohols are illustrated in Supplementary Fig. 7. A consistent degree of superheat of 30°C was kept for all the sugar alcohol PCMs, i.e., the heating temperatures were 150°C, 200°C, 220°C, and 255°C for erythritol, d-mannitol, d-dulcitol, and inositol, respectively. The erythritol, possessing the lowest melting point at ~118°C, exhibits the most superior thermal stability among the evaluated sugar alcohol-based materials, whereas inositol, having the highest melting point at ~225°C, displays the most pronounced susceptibility to thermal degradation.

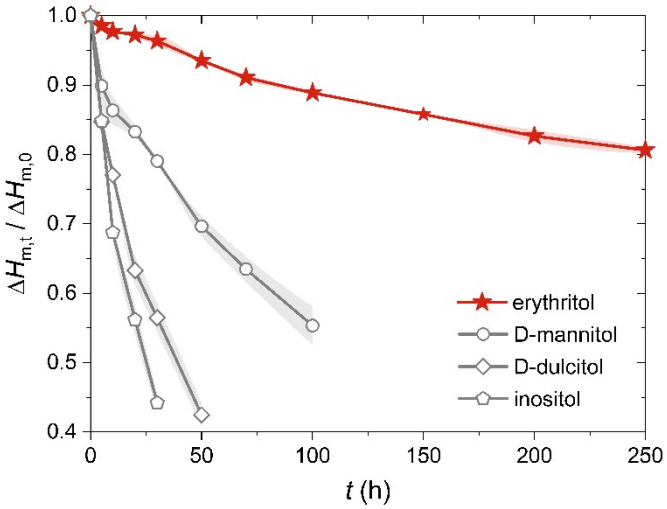

Supplementary Fig. 7. Changes in the melting enthalpy for erythritol, D-mannitol, D-dulcitol, and inositol when heated at a consistent superheat of 30°C.

As shown in Supplementary Fig. 8a, upon heating the pure D-mannitol for 100 h at the degrees of superheat of 10°C, 20°C and 30°C, its melting enthalpy declines to 217.7, 193, and 154.9 J/g, respectively. In contrast, the incorporation of 1 wt.% AO1010 effectively mitigates this

degradation, yielding higher retained enthalpies of 242.2, 223.6, and 160.3 J/g under the same conditions. Analysis of these results reveals that while AO1010 provides appreciable stabilization at lower degrees of superheat, its protective efficacy is virtually negated at a 30°C superheat, where the accelerated degradation kinetics likely exceeds the antioxidant's buffering capacity.

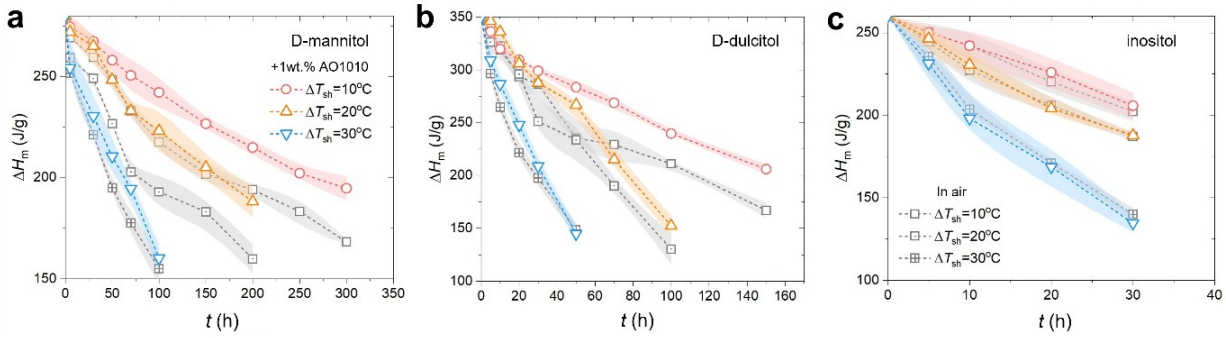

Supplementary Figure 8. Changes in the melting enthalpy of other sugar alcohols at various degrees of superheat (i.e., 10°C, 20°C, and 30°C) with and without 1 wt.% AO1010 protection: (a) D-mannitol, (b) D-dulcitol and (c) inositol.

The stabilization effect of AO1010 on D-dulcitol is in consistent with that observed for D-mannitol. At lower superheat levels (10°C and 20°C), AO1010 provides a discernible protective barrier, with the stabilized samples maintaining significantly higher melting enthalpies than their pristine counterparts (Supplementary Fig. 8b). However, once the degree of superheat reaches 30°C, the antioxidant's ability to enhance thermal stability is entirely compromised. In certain instances, we even observed a negative effect, where the melting enthalpy of the AO1010-stabilized sample drops below that of the pristine D-dulcitol.

AO1010 has limited effectiveness in improving the thermal stability of inositol and, in certain

cases, paradoxically speeds up its degradation (see Supplementary Fig. 8c). This phenomenon is primarily attributed to two factors: first, the melting point of inositol aligns with the thermal decomposition threshold of AO1010, leading to the additive's own pyrolysis. More crucially, the intrinsic pyrolysis rate of inositol at this elevated temperature is sufficiently aggressive to overwhelm the stabilization kinetics of the antioxidant, rendering the protection mechanism ineffective

Supplementary Note 7: Calculation of the energy density of erythritol

The total heat stored/released by a PCM consists of three components: sensible heat in the solid phase, sensible heat in the liquid phase, and latent heat associated with phase transition, as given by

$$Q = c_{\mathrm{l}} m \Delta T_{\mathrm{l}} + m \Delta H_{\mathrm{m}} + c_{\mathrm{s}} m \Delta T_2 \quad \text{(S-4)}$$

where Q is the total heat released by the PCM (Wh), c_{l} and c_{s} are the specific heat capacities of the liquid and solid phases, respectively (kJ/kg • K), ΔT_1 is the temperature difference between the heated boundary and the melting point (K), ΔT_2 is the temperature difference between the melting point and the cooled boundary, and m is the mass of the PCM (kg). The amount of heat stored per unit mass represents the energy density (Wh/kg).

In this work, we calculated the total heat based on cooling at 40°C and heating at 148°C (i.e., ~30°C superheat for erythritol). Given that its solid specific heat capacity is 1.38 kJ/kg·K, liquid specific heat capacity is 2.76 kJ/kg·K, and its melting point is 118°C, the calculated energy density of erythritol is 144.6 Wh/kg.

Supplementary Note 8: Test apparatus and procedure for cyclic stability

The schematic and photographic views of the thermal cycling experimental setup are presented in Supplementary Fig. 9a and b, respectively. The apparatus is primarily composed of a reaction vessel for housing the PCMs, a vacuum system integrated with a nitrogen gas manifold for inert atmosphere protection, and a centralized unit for temperature control and data acquisition.

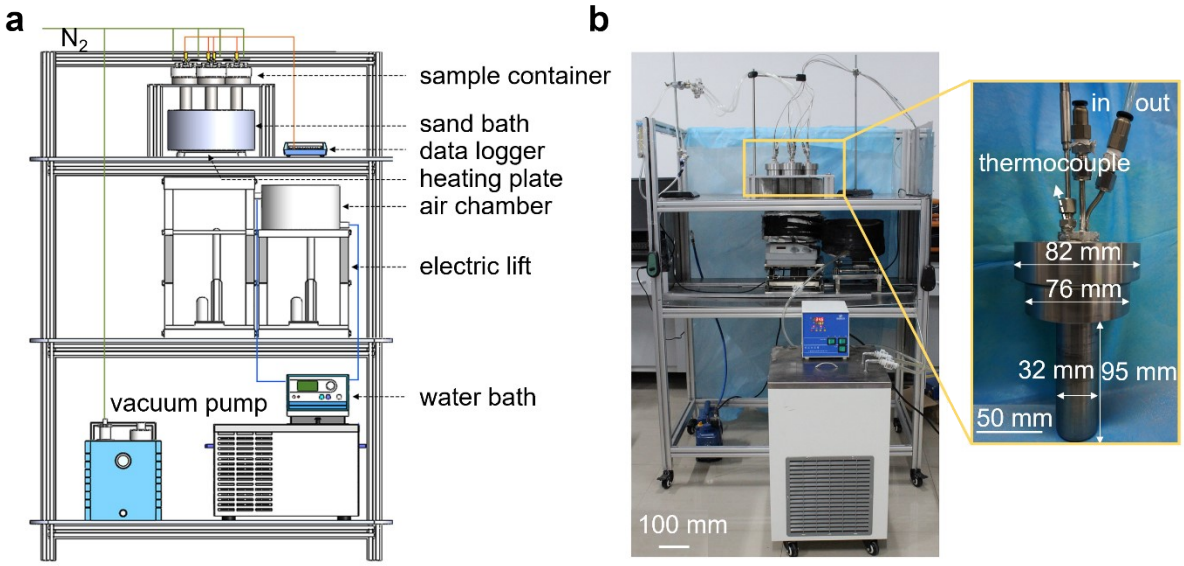

Supplementary Fig. 9. Experimental setup for thermal cycling stability testing: (a) schematic diagram and (b) photographic view of the apparatus.

The lower section of the reaction vessel consists of a test tube with an outer diameter of 32 mm, a wall thickness of 2 mm, and a length of 95 mm. The mid-section features a ring-shaped component with an outer diameter of 76 mm and a thickness of 6 mm, which is integrated with the lower tube through precision welding. The outer surface of this ring is threaded to facilitate connection with a sealing cap. The dimensions of the sealing cap—comprising its outer diameter,

thickness, and height—were specifically designed at 82 mm, 6 mm, and 25 mm, respectively. To enhance the sealing integrity, a graphite gasket was recessed into the internal top surface of the sealing cap.

Two stainless steel tubes were coupled to the cap via threaded connections, enabling the thermal cycling tests to be conducted under both ambient air and inert atmospheres. The right-hand conduit of the reaction vessel was connected to a vacuum pump (VALUE, V-i140SV) and a gas cylinder for evacuation and the introduction of protective gas, while the left-hand tube serves as the exhaust outlet. Furthermore, a T-type thermocouple was vertically secured along the central axis of the sealing cap to monitor the temperature evolution of the PCM during the heat charging and discharging cycles. The sensing junction of the thermocouple was positioned 5 mm above the internal base of the test tube.

The thermal cycles were performed by a digital hotplate (MS7-H550-S) and a recirculating water bath (DC-1015) for the heating and cooling phases, respectively. During the heating stage, the reaction vessel was immersed in a sand bath situated on the hotplate, which was filled with small monodispersed alumina particles. For the cooling stage, the dual-layered cylindrical stainless-steel chamber, temperature-regulated by the water bath, provides a stable natural convection environment for the PCM. To facilitate the seamless transition of the reaction vessel between the sand bath and the cooling chamber, two electric laboratory jacks were positioned beneath the hotplate and the cylindrical vessel. The thermal cycling procedure was initiated by raising the hotplate-mounted sand bath to immerse the test tube, thereby melting the sample. Upon complete fusion, the sand bath was lowered to separate it from the tube and then translated laterally

to the right. Subsequently, another lift moves the low-temperature constant-temperature chamber beneath the test tube, raising it until the tube was fully submerged to initiate the cooling phase. The completion of this cooling stage marked the end of one full melting-solidification cycle.

Supplementary References:

1. X. Shao, S. Yang, H. Shi, L. Fan, Y. Yuan, A comprehensive evaluation on the cycling stability of sugar alcohols for medium-temperature latent heat storage, *J. Energy Storage* 64 (2023) 107190.
2. K. Wusiman, T.H. Wang, L. Shi, et al. A novel evaluation method for thermal stability of erythritol as phase change materials. *Therm. Sci. Eng. Prog.* 59 (2025) 103303.
3. A. Solé, H. Neumann, S. Niedermaier, et al. Stability of sugar alcohols as PCM for thermal energy storage. *Sol. Energy Mater. Sol. Cells* 126 (2014) 125–134.
4. H. Che, Q. Chen, Q. Zhong, et al. The effects of nanoparticles on morphology and thermal properties of erythritol/polyvinyl alcohol phase change composite fibers. *E-Polymers* 18 (2018) 321–329.
5. C.P. Patel, T. Pavankumar, A. Narla, et al. Experimental study of a latent heat thermal energy storage system using erythritol for medium temperature applications. *Case Stud. Therm. Eng.* 53 (2024) 103907.
6. J.D. Kocher, J. Woods, A. Odukomaiya, et al. Thermal battery cost scaling analysis: minimizing the cost per kWh. *Energy Environ. Sci.* 17 (2024) 2206–2218.
7. J.W. Lim, M. Day, S. Cui, et al. Iso-cost-performance of thermal energy storage. *J. Phys. Energy* 8 (2026) 011001.